Atmospheric Research 344 (2027) 109329



Contents lists available at ScienceDirect

Atmospheric Research

journal homepage: www.elsevier.com/locate/atmosres





Long-term CALIOP observations of vertical aerosol stratification over Shanghai: Meteorological modulation and height-resolved transport

Fangzhi Wei [a,b], Tianwen Wei [a,b,*], Qiuwei Xia [c], Yiqian Liu [a,b], Xinming Zhu [a,b], Haiyun Xia [a,b,c]

[a] State Key Laboratory of Climate System Prediction and Risk Management, Nanjing University of Information Science and Technology, Nanjing 210044, China
[b] School of Atmospheric Physics, Nanjing University of Information Science and Technology, Nanjing 210044, China
[c] Institute of Lidar Technology, GuangZai Co., Ltd., Hangzhou 310005, China

ARTICLE INFO

Keywords:
CALIOP
Vertical aerosol stratification
Boundary-layer-relative aerosol layers
Height-resolved transport

ABSTRACT

Aerosol vertical distribution is essential for assessing aerosol radiative effects, interpreting aerosol optical depth, and understanding aerosol-boundary-layer interactions. However, how meteorological conditions modulate height-resolved aerosol layers over coastal megacities remains insufficiently quantified. Here, we examine aerosol vertical stratification over Shanghai using CALIOP overpasses from 2006 to 2023, together with ERA5 meteorological fields, 925-hPa circulation-regime classification, and HYSPLIT/WPSCF diagnostics. The observations reveal a persistent three-layer aerosol structure within 0–8 km: a polluted/marine mixed layer below 2 km, an elevated 2–4 km layer with pronounced elevated-smoke and pollution-related aerosol signals, and a dust-related layer at 4–8 km. Although aerosol optical loading is largest below 2 km, layers above 2 km contribute 44.2% of the 0–8 km AOD_{532}, indicating that elevated aerosols are an important component of the column optical signal over Shanghai. Among the meteorological factors examined, PBLH shows the clearest relationship with aerosol vertical redistribution, with higher PBLH associated with a larger relative aerosol-sample share below 2 km and smaller shares above 2 km. Relationships involving vertical motion, lower-tropospheric stability, ventilation, and relative humidity vary more strongly with altitude and season. The 925-hPa circulation classification further identifies a weak-gradient transition regime associated with greater aerosol optical loading and a pronounced 2–4 km elevated-smoke peak. For CALIOP-detected aerosol layers with bases above the PBLH and vertical ranges extending into the 2–4 km altitude band, height-resolved WPSCF indicates vertically stratified potential transport pathways. The most coherent event-related high-WPSCF region occurs within the 2–4 km layer over central-eastern China and the western YRD, whereas 4–8 km signals indicate additional upstream high-altitude pathways from North China, Inner Mongolia, and northwestern inland China. Near-surface high-WPSCF cells are sparse and spatially discontinuous. These findings show that aerosol vertical placement and transport height should be considered when interpreting column AOD and evaluating modeled aerosol vertical profiles over coastal megacities.

1. Introduction

Aerosols are an integral component of the atmospheric environment and climate system. By scattering and absorbing radiation, serving as cloud condensation nuclei, and participating in atmospheric chemical processes, aerosols can affect air quality, radiative balance, cloud microphysics, and regional weather and climate (Andreae and Crutzen, 1997; Haywood and Boucher, 2000; Kaufman et al., 2002; Mülmenstädt and Feingold, 2018). These effects depend not only on near-surface aerosol concentrations and horizontal distributions, but also critically on their vertical distribution. For example, absorbing aerosols can exert substantially different radiative effects and stability responses when located at different altitudes (Kaufman et al., 2002; Li et al., 2017; Samset et al., 2013). Aerosols within the boundary layer are generally influenced by local emissions, turbulent mixing, wet scavenging, and near-surface transport, whereas aerosol layers above the boundary layer

* Corresponding author at: State Key Laboratory of Climate System Prediction and Risk Management, Nanjing University of Information Science and Technology, Nanjing 210044, China.
E-mail address: twwei@nuist.edu.cn (T. Wei).

https://doi.org/10.1016/j.atmosres.2026.109329
Received 14 June 2026; Received in revised form 25 July 2026; Accepted 7 September 2026
Available online 12 September 2026
0169-8095/© 2026 Elsevier B.V. All rights are reserved, including those for text and data mining, AI training, and similar technologies.

are more often associated with residual-layer processes, regional transport, boundary-layer-free-troposphere exchange, or long-range transport (Bourgeois et al., 2018; Fan et al., 2019). Consequently, neither near-surface observations nor column-integrated aerosol optical depth (AOD) alone can determine whether aerosols are primarily confined within the boundary layer, distributed in elevated layers, or present in the lower free troposphere. This limitation also partly explains the frequent mismatch between AOD and near-surface particulate pollution (He et al., 2021; Wang and Christopher, 2003; Zhu et al., 2024b).

Spaceborne lidar observations are essential for characterizing aerosol vertical structure over long time periods and across regional to global scales. The Cloud-Aerosol Lidar with Orthogonal Polarization (CALIOP) aboard the CALIPSO satellite provides vertically resolved profiles of clouds and aerosols and has been widely used to examine the three-dimensional distribution of tropospheric aerosols at global and regional scales, including near-surface accumulation, elevated aerosol transport, and height-dependent variations in aerosol classification (Gui et al., 2021; Guo et al., 2016; Winker et al., 2009, 2013). The CALIPSO Version 4 products introduced important updates in cloud-aerosol discrimination, aerosol subtype classification, and lidar-ratio selection. In particular, Version 4 added the dusty marine subtype and revised the classification logic for several tropospheric aerosol subtypes, thereby providing a more consistent framework for long-term analyses of aerosol vertical structure (Kim et al., 2018).

Previous CALIOP-based studies have examined aerosol vertical distributions through long-term climatological analyses, regional comparisons, and urban-cluster investigations. Long-term analyses at global and regional scales have characterized type-dependent aerosol occurrence, altitude-resolved optical loading, temporal trends, and meteorological variability (Gui et al., 2021). Over China, long-term CALIOP records have been used to investigate changes in aerosol vertical distributions and transport pathways across representative regions, including the Yangtze River Delta (YRD) (Chen et al., 2023a), while studies of major urban clusters in eastern China have analyzed aerosol-subtype occurrence and extinction profiles under different meteorological and air-mass conditions (Liu et al., 2021b). Over the coastal YRD, CALIOP observations have also been used to examine seasonal variations in aerosol types, optical properties, and transport pathways (Reddy et al., 2019).

Shanghai is influenced by local and regional emissions, marine air masses, and synoptic transport, which can produce altitude-dependent aerosol signals. Previous studies have related seasonal aerosol profiles to air-mass movements and surface $PM_{2.5}$ concentrations (Wang et al., 2020), documented contrasting vertical distributions during haze and floating-dust events (Liu et al., 2016), characterized long-term variations in aerosol optical properties (Liu et al., 2021a), and linked elevated aerosol layers to regional and long-range transport (Fan et al., 2019). Stagnation, land–sea-breeze circulations, urban heat-island effects, and regional recirculation have also been associated with pollutant accumulation and transport over Shanghai and its surrounding regions (He et al., 2022; Hu et al., 2022; Lu et al., 2023; Shen et al., 2019). However, these studies have generally focused on individual events, single-site measurements, or specific processes, leaving the long-term integrated vertical organization of aerosols over Shanghai insufficiently characterized.

A long-term, integrated understanding of how aerosol-subtype composition, optical properties, and aerosol-layer geometry jointly define the vertical organization of the 0–8 km aerosol column over Shanghai is still lacking. It also remains unclear how this organization varies with meteorological conditions and low-level circulation regimes and how elevated aerosol layers are linked to transport pathways at different heights. Clarifying these relationships is important for interpreting column–surface aerosol discrepancies and evaluating modeled aerosol vertical profiles.

Here, we use CALIOP observations during 2006–2023 to investigate aerosol vertical stratification over Shanghai. We integrate CALIOP aerosol-subtype occurrence, APro optical profiles, ALay layer geometry, ERA5 meteorological conditions, objective 925-hPa circulation regimes, and height-resolved HYSPLIT/WPSCF diagnostics to characterize the vertical organization of the 0–8 km aerosol column and its meteorological and transport associations. By combining these complementary components within a unified analytical framework, this study provides long-term spaceborne-lidar evidence for interpreting aerosol vertical organization, column–surface aerosol discrepancies, and modeled aerosol vertical profiles over a coastal megacity.

2. Data and methods

2.1. Study region

The study domain spans 120.85–122.20°E and 30.67–31.88°N, covering Shanghai and the nearby Yangtze River estuary-coastal zone. Shanghai is situated in the eastern YRD, where the Yangtze River estuary meets the western margin of the East China Sea. Aerosol variability over Shanghai reflects the combined effects of local emissions, regional transport, marine inflow, and coastal boundary-layer meteorology, making the region a suitable setting for examining aerosol vertical stratification and height-dependent transport over a coastal megacity.

This study focuses on the 0–8 km altitude range. This range spans boundary-layer and lower-to-middle tropospheric altitudes, allowing the analysis to distinguish aerosol signals confined to the lower layer from those occurring above the planetary boundary layer.

2.2. CALIOP products and aerosol occurrence metrics

We use CALIOP Level 2 Version 4.51 standard products from CALIPSO overpasses that intersect the Shanghai domain from June 2006 to June 2023. The datasets include the Vertical Feature Mask (VFM; CAL_LID_L2_VFM-Standard-V4–51), the 5-km Aerosol Profile (APro; CAL_LID_L2_05kmAPro-Standard-V4–51), and the 5-km Aerosol Layer (ALay; CAL_LID_L2_05kmALay-Standard-V4–51). The VFM product is used to identify aerosol features, obtain CALIOP-assigned aerosol subtypes, and characterize their vertical distribution (Jing et al., 2025). The APro product provides vertical profiles of aerosol optical properties, including the 532-nm aerosol extinction coefficient and particulate depolarization ratio (Young and Vaughan, 2009). The ALay product is used to obtain layer-scale properties, including layer base height, layer top height, geometric midlayer height, layer thickness, and layer-integrated 532-nm aerosol optical depth (AOD_{532}) (Wu et al., 2025; Zha et al., 2024).

Although aerosol-layer boundaries can be inferred from APro profiles, doing so requires a study-specific threshold or segmentation criterion. We therefore use the ALay base, top, and thickness descriptors generated by the CALIOP Level-2 multiresolution feature-detection algorithm (Vaughan et al., 2009). Weak features may require longer along-track averaging and therefore have coarser effective horizontal resolution and greater boundary uncertainty. Within 0–8 km, APro profiles are reported on a 5-km along-track and 60-m vertical grid; because weak features may have coarser effective along-track resolution, APro is used for long-term composites and broad layer-integrated optical diagnostics rather than fine-scale variability in individual records.

Only VFM samples classified as aerosols are retained and grouped into the seven CALIOP Version 4 tropospheric subtypes: clean marine, dust, polluted continental/smoke, clean continental, polluted dust, elevated smoke, and dusty marine. These algorithm-derived optical categories depend on aerosol optical properties, layer altitude, surface type, and geographic information and are not direct measures of chemical composition or emission sources. In particular, elevated smoke and polluted continental/smoke should not be interpreted as proxies for black carbon or other specific chemical components (Kim et al., 2018). After spatial screening, temporal matching, and product-level quality control, 854 valid CALIPSO overpasses are retained for analysis.

To quantify the relative vertical distribution of aerosol subtypes within 0–8 km, we define ALL_FO as the subtype-altitude share among all valid aerosol samples in this altitude range (Liu et al., 2021a, 2021b):

$$ALL_FO_{s,z} = \frac{N_{s,z}}{\sum_s \sum_z N_{s,z}} \times 100\% \quad (1)$$

where $N_{s,z}$ denotes the number of samples identified as aerosol subtype s in altitude bin z. The summation is performed over all aerosol subtypes and all altitude bins within 0–8 km. Because clear-air samples are excluded from the denominator, ALL_FO represents the relative share of each subtype–altitude bin among detected aerosol samples within the 0–8 km column, rather than the absolute aerosol occurrence probability relative to all atmospheric samples. The denominator is recalculated for each season, meteorological group, and circulation regime; consequently, a higher ALL_FO value may reflect more detected samples in that bin, fewer samples in other bins, or both. It should therefore not be interpreted independently as an increase in the absolute occurrence of a subtype or altitude layer. For the ALay analysis, only aerosol layers with CAD scores between −100 and − 20 are retained to reduce the influence of cloud contamination and feature misclassification (Liu et al., 2009).

2.3. ERA5 meteorological matching and regime-based diagnostics

ERA5 hourly pressure-level and single-level fields on a 0.25° × 0.25° latitude–longitude grid are used to characterize the meteorological conditions associated with each CALIPSO overpass (Hersbach et al., 2020). The two ERA5 hourly fields bracketing the corresponding CALIPSO scan time are linearly interpolated in time to the exact UTC overpass time. The temporally interpolated fields are then bilinearly interpolated to the latitude and longitude of each valid CALIOP profile within the Shanghai domain; nearest-neighbor values are used only when bilinear interpolation is unavailable or produces missing values. For the meteorological-group analyses, the matched profile-level values are averaged to obtain one representative value for each overpass.

Five meteorological variables are selected to represent key processes relevant to aerosol vertical structure. Planetary boundary layer height (PBLH) represents the vertical extent of boundary-layer mixing. Vertical velocity in pressure coordinates at 750 hPa (PVV) is used as an indicator of large-scale vertical motion, with negative values indicating ascent and positive values indicating subsidence. Relative humidity at 925 hPa (RH) is used to characterize near-boundary-layer moisture conditions. Lower-tropospheric stability (LTS) is defined as the potential-temperature difference between 700 and 1000 hPa and is used to characterize lower-troposphere thermal stability and the potential inhibition of vertical exchange between the boundary layer and the free troposphere (Wood and Bretherton, 2006):

$$\mathrm{LTS} = \theta_{700} - \theta_{1000} \quad (2)$$

where θ_{700} and θ_{1000} are the potential temperatures at 700 and 1000 hPa, respectively. Larger LTS indicates a more stable lower troposphere.

The ventilation coefficient (VC) is used to represent the combined effect of boundary-layer depth and horizontal wind speed. It is calculated by integrating the wind speed within the boundary layer (Zong et al., 2023):

$$VC = \frac{1}{1000} \int_0^{PBLH} \sqrt{u(z)^2 + v(z)^2}\, dz \quad (3)$$

where $u(z)$ and $v(z)$ are the zonal and meridional wind components at height z, respectively, and PBLH denotes the planetary boundary layer height. VC therefore reflects boundary-layer ventilation by combining mixing depth and horizontal transport capacity, and is interpreted as a proxy for aerosol dilution potential within the boundary layer.

For the profile-composite analyses, PBLH, LTS, RH, and VC are divided into low, moderate, and high groups based on their terciles across all CALIPSO overpass cases. PVV is grouped by sign into ascending-motion (PVV < 0) and subsiding-motion (PVV > 0) conditions. These groupings are used to compare subtype-specific ALL_FO profiles under different meteorological conditions.

To reduce the influence of seasonal sampling differences in the pooled overpass dataset, we further apply a season-controlled high-minus-low diagnostic. Within each season, each meteorological variable is divided into low and high groups using the lower and upper terciles of its seasonal distribution. To provide a common vertical framework for the subsequent analyses, three broad altitude bands were defined from coherent transitions in the long-term mean aerosol-subtype occurrence and optical-property profiles and were then held fixed throughout the meteorological, circulation-regime, and transport diagnostics. The observational basis for these boundaries is presented in Section 3.1. For each variable, the median high-minus-low difference in layer-integrated ALL_FO is then calculated for three altitude ranges: 0–2, 2–4, and 4–8 km. The resulting seasonal differences are then averaged across the four seasons to obtain the season-controlled layer difference, $\Delta_{m,z}$, for meteorological variable m and altitude layer z. In this diagnostic, PVV is also grouped using seasonal terciles. Therefore, the high-minus-low PVV difference represents the contrast between higher- and lower-PVV conditions, rather than a simple subsidence-minus-ascent comparison.

For a given meteorological variable m, the vertical redistribution strength is defined as

$$R_m = \frac{1}{2} \sum_z \left| \Delta_{m,z} \right| \quad (4)$$

where z denotes one of the three altitude layers: 0–2, 2–4, and 4–8 km. The factor of 1/2 avoids double-counting compensating increases and decreases among layers, so Rm represents the total amplitude of vertical redistribution in layer-integrated ALL_FO. It is interpreted as a statistical diagnostic of redistribution strength, rather than as a causal contribution rate.

Uncertainty arising from the finite number of CALIPSO overpasses is estimated using a seasonally stratified bootstrap. Within each season, CALIPSO overpass cases are resampled with replacement, and the complete season-controlled diagnostic procedure is repeated 1000 times. The 2.5th and 97.5th percentiles of the resulting bootstrap distribution are used to define the 95% confidence interval. A high-minus-low difference is considered robust in sign when its 95% confidence interval does not include zero.

Because ALL_FO describes relative aerosol-sample distribution rather than optical loading, we perform an optical consistency check using APro 532-nm aerosol extinction profiles. Layer-integrated extinction and the fractional contribution of each altitude layer to the 0–8 km AOD_{532} are calculated for the same altitude ranges and analyzed using the same season-controlled high-minus-low framework. The APro-based optical diagnostics are used to assess whether the relative redistribution inferred from ALL_FO is accompanied by corresponding changes in vertically resolved optical contribution. They are not used to convert ALL_FO into aerosol mass concentration or to infer absolute aerosol mass loading.

2.4. Objective Classification of Low-Level Circulation Regimes

To characterize the regional low-level circulation background of each CALIPSO overpass, we perform an objective regime classification using ERA5 925-hPa zonal wind, meridional wind, and geopotential height. The classification domain is defined as 110–128°E and 25–40°N, covering the YRD, the East China coastal region, and major upstream sectors that potentially influence transport to Shanghai. Compared with surface winds, the 925-hPa level is less directly affected by near-surface friction and therefore better represents regional transport direction, low-level wind variability, and synoptic-scale circulation patterns (Liu et al., 2019).

For each CALIPSO overpass, the corresponding ERA5 u, v, and Z fields are extracted at the matched overpass time. The spatial fields are first weighted by the cosine of latitude and then standardized to place variables with different units and variances on comparable scales. Principal component analysis (PCA) is then applied for dimensionality reduction, and K-means clustering is performed on the retained leading principal-component scores. The number of clusters is selected by combining standard clustering metrics, cluster-size constraints, and the physical interpretability of the resulting composite circulation patterns. Similar PCA-k-means approaches have been used in previous studies to identify circulation regimes associated with particulate pollution (Chang and Zhan, 2017).

2.5. Aerosol Layer Event Definition and Height-Resolved WPSCF Analysis

In the ALay-based layer-structure analysis, aerosol layers within 0–8 km are classified according to the position of their layer bases relative to the ERA5 PBLH matched to each CALIOP profile. Layers with bases above the matched PBLH are defined as above-PBL-base (APB) layers, whereas layers with bases at or below the matched PBLH are defined as within-PBL-base (WPB) layers. This classification is geometric and does not by itself demonstrate dynamical decoupling from the boundary layer.

For geometric and optical layer-property statistics, only one dominant layer is retained for each layer-base category within each CALIOP profile. When multiple aerosol layers of the same layer-base category occur within a profile, the layer with the largest AOD_{532} is selected as the dominant layer. This avoids overweighting multilayer profiles in the layer-property statistics. For the i-th CALIPSO overpass in the ALay analysis, the profile-level occurrence of layer category c within altitude band k is defined as

$$O_i^{c,k} = \frac{n_i^{c,k}}{N_i} \tag{5}$$

where c denotes the boundary-layer-relative layer category, including APB and WPB layers, and k denotes the target altitude band; Here, $n_i^{c,k}$ is the number of valid CALIOP profiles that contain at least one aerosol layer whose base-defined category is c and whose vertical extent intersects altitude band k. N_i is the total number of profiles included in the ALay statistics for that overpass after valid PBLH matching.

Following the vertical framework identified from the long-term profiles, the profile occurrence of APB layers overlapping the 2–4 km altitude band is first calculated. A case is identified as a 2–4 km APB-layer event when

$$O_i^{APB,2-4\,km} \geq P_{75}^{+} \tag{6}$$

where P_{75}^{+} denotes the 75th percentile calculated from overpasses with $O_i^{\mathrm{APB},2-4\,\mathrm{km}} > 0$, across all CALIPSO overpasses in the ALay analysis. These cases constitute the 2–4 km APB-layer event subset for WPSCF analysis.

The HYSPLIT backward trajectories are driven by the NOAA Air Resources Laboratory GDAS1 meteorological archive, which provides global $1^\circ \times 1^\circ$ meteorological fields at 3-h intervals. For each CALIPSO overpass case, trajectories are initialized at the Shanghai receptor location at the corresponding CALIPSO overpass time and calculated backward for 48 h (Stein et al., 2015). The trajectory calculations are interpreted as kinematic air-parcel pathways driven by the GDAS1 meteorological fields. Trajectory clustering and WPSCF are treated separately. Clustered trajectories at 500, 1500, 3000, and 6000 m are used only to summarize the general height dependence of air-mass pathways. The WPSCF analysis for 2–4 km APB-layer events uses an arrival-height ensemble of 2500, 3000, and 3500 m. For a given event category, $n_{ijh}$is the total number of trajectory points from all valid CALIOP overpass cases passing through grid cell (ij)within altitude layer h, whereas $m_{ijh}$is the number of trajectory points from the selected event cases passing through the same grid cell and altitude layer.

$$\mathrm{PSCF}_{ijh} = \frac{m_{ijh}}{n_{ijh}} \tag{7}$$

Trajectory points are further grouped into four altitude layers: 0–1, 1–2, 2–4, and 4–8 km. The 2–4 km APB layer is used to define the event category, whereas the 0–1, 1–2, 2–4, and 4–8 km trajectory layers are used to diagnose the potential transport pathways associated with these events at different heights.

To suppress spuriously high PSCF values in sparsely sampled grid cells, an empirical weighting factor W_{ijh} is applied:

$$\mathrm{WPSCF}_{ijh} = \mathrm{PSCF}_{ijh} \times W_{ijh} \tag{8}$$

The weighting function is defined separately for each trajectory altitude layer using the mean number of denominator endpoints per grid cell, $n_{\mathrm{ave},h}$:

$$W_{ijh} = \begin{cases} 1.00, & n_{ijh} > 3.0n_{\mathrm{ave},h}, \\ 0.70, & 1.5n_{\mathrm{ave},h} < n_{ijh} \leq 3.0n_{\mathrm{ave},h}, \\ 0.42, & 1.0n_{\mathrm{ave},h} < n_{ijh} \leq 1.5n_{\mathrm{ave},h}, \\ 0.05, & n_{ijh} \leq 1.0n_{\mathrm{ave},h}. \end{cases} \tag{9}$$

The height-resolved WPSCF is applied as a vertical extension of the conventional PSCF method to identify potential transport regions in different altitude layers (Kim et al., 2016; Dimitriou et al., 2021). The weighting correction reduces the influence of grid cells with limited trajectory-point coverage (Polissar et al., 2001).

3. Results

3.1. Vertical aerosol stratification and seasonal variability over Shanghai

Fig. 1 presents the long-term mean vertical structure of CALIOP aerosol subtype occurrence and optical properties over Shanghai during 2006–2023. The aerosol subtypes exhibit clear altitude-dependent differentiation within 0–8 km (Fig. 1a). Below 2 km, polluted dust, polluted continental/smoke, clean marine, and dusty marine show relatively high ALL_FO values, indicating a lower-layer mixture of pollution-, dust-, and marine-associated CALIOP subtype signatures. The elevated-smoke subtype peaks at approximately 2–3 km, marking a distinct elevated aerosol feature, whereas the dust subtype maintains relatively high ALL_FO values at 4–6 km, consistent with possible middle-to-upper-level dust transport influence. Based on the subtype occurrence profiles, the vertical aerosol structure over Shanghai can be broadly characterized by a lower polluted/marine mixed layer, a 2–4 km elevated aerosol layer, and a 4–8 km dust-related layer.

The optical profiles further support the subtype-based stratification (Fig. 1b-d). The 532-nm aerosol extinction coefficient is largest below 2 km and generally decreases with altitude, indicating that the lower troposphere dominantes aerosol optical loading over Shanghai. In contrast, particulate depolarization increases above 4 km, supporting a larger nonspherical-particle contribution in the dust-related upper layer. Layer-resolved AOD_{532} shows that the 0–2, 2–4, and 4–8 km layers contribute 55.8%, 23.9%, and 20.3% of the total 0–8 km optical signal, respectively. Thus, aerosols above 2 km together account for 44.2%, demonstrating that elevated and middle-to-upper-level aerosols are a substantial component of the column optical signal.

These dust-related features are consistent with previous lidar studies. Long-term CALIOP observations over eastern China showed an elevated-smoke maximum near 3 km and dust occurrence throughout the 0–8 km column (Liu et al., 2021b), while Tian et al. (2017) identified middle- and upper-tropospheric long-range dust transport over China. By contrast, event-based ground-lidar observations in Shanghai found that more than 85% of aerosols during haze and floating-dust events occurred below 1 km (Liu et al., 2016). This difference likely reflects the sampling frameworks: event studies emphasize surface-reaching

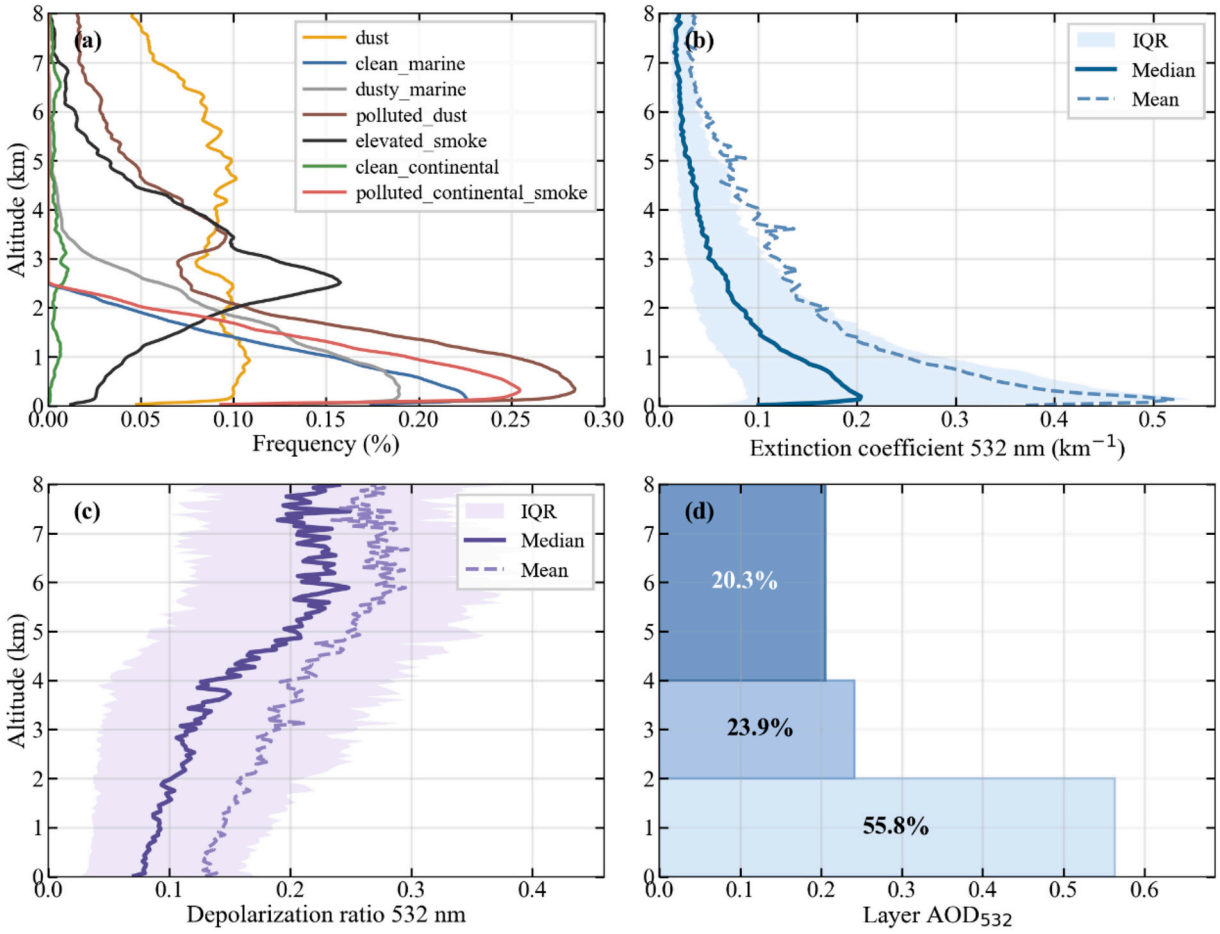


Fig. 1. Long-term mean vertical structure of CALIOP aerosol subtype occurrence and optical properties over Shanghai during 2006–2023. (a) ALL_FO profiles for aerosol subtypes; (b) 532-nm aerosol extinction coefficient; (c) 532-nm particulate depolarization ratio; and (d) layer-resolved AOD_{532} for 0–2, 2–4, and 4–8 km. Shading in (b) and (c) denotes the interquartile range, with solid and dashed lines indicating the median and mean, respectively. Labels in (d) indicate each layer's contribution to the total 0–8 km AOD_{532}.

episodes, whereas the 2006–2023 CALIOP climatology also captures lofted dust layers that may remain decoupled from the surface.

Together, the long-term mean aerosol-subtype occurrence, extinction, and particulate-depolarization profiles support a three-layer framework: a lower polluted/marine mixed layer below 2 km, an elevated aerosol layer at 2–4 km, and a dust-related layer at 4–8 km. The 2 km boundary separates the lower layer dominated by pollution- and marine-associated subtype signals from the distinct elevated-smoke maximum at approximately 2–3 km, whereas the 4 km boundary marks the transition toward stronger dust-related occurrence and particulate depolarization aloft. The 2–4 km interval is of particular interest because it contains pronounced elevated-smoke and pollution-related signals, contributes 23.9% of the total 0–8 km optical signal, and forms a distinct elevated feature above the lower polluted/marine-dominated layer. These *AOD* fractions describe relative optical contributions and should not be interpreted as proportional aerosol mass burdens.

Seasonal profiles show that the three-layer structure varies systematically by season rather than remaining unchanged throughout the year (Fig. 2). Spring and winter are characterized by stronger dust-related signals aloft, especially within 4–6 km, together with enhanced polluted-dust or dusty-marine subtype signals in the lower layer. Summer shows the most pronounced elevated-smoke peak at 2–4 km and stronger lower-layer marine/pollution-associated subtype signatures. Autumn exhibits a weaker elevated-smoke peak and acts as a transitional season between the summer elevated-layer maximum and the spring-winter dust-related upper-layer enhancement. Thus, seasonality primarily alters aerosol-subtype composition within a persistent three-layer framework rather than the framework itself.

3.2. *Meteorological modulation of vertical aerosol redistribution*

This section examines how the relative vertical distribution of CALIOP aerosol subtypes within 0–8 km varies across the meteorological groupings defined in Section 2.3. Because ALL_FO is normalized within each meteorological group using detected aerosol samples only, the following differences describe relative subtype–altitude composition rather than absolute aerosol occurrence, mass concentration, or column loading. The meteorological variables are therefore treated as diagnostic groupings rather than causal factors.

PBLH shows the clearest and most seasonally consistent association with the vertical distribution of aerosol subtype shares (Figs. 3a-c and Fig. 5). Under low-PBLH conditions, elevated smoke forms a pronounced 2–4 km peak, while polluted dust and dust retain non-negligible shares above 2 km. From low- to high-PBLH groups, the relative aerosol-sample share increases within 0–2 km and generally decreases above 2 km. This pattern shift is further evaluated using the season-controlled diagnostic in Fig. 5.

The profile response associated with VC is similar in direction to that associated with PBLH, but is less seasonally consistent (Figs. 3d-f). Under low-VC conditions, elevated smoke retains a distinct 2–4 km peak, while polluted dust extends from the lower layer into the middle

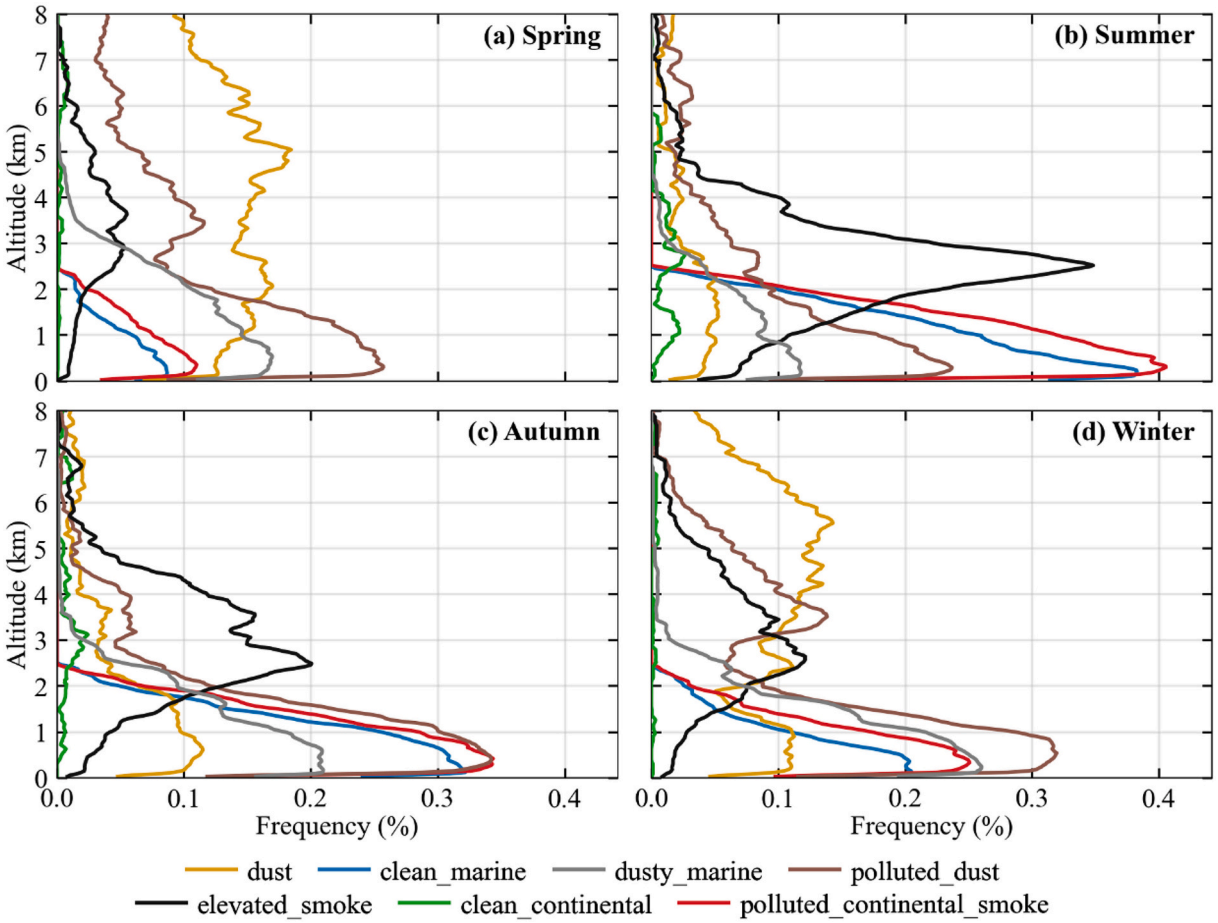


Fig. 2. Seasonal vertical distributions of CALIOP aerosol subtype ALL_FO over Shanghai during 2006–2023. Panels show (a) spring, (b) summer, (c) autumn, and (d) winter.

troposphere, indicating a more vertically distributed subtype composition. Under high-VC conditions, several subtypes have larger shares in the lower layer and reduced shares above 2 km. However, the season-stratified diagnostic indicates that VC-related differences are mainly confined to summer and autumn and to the 0–4 km layer (Fig. S1). VC is therefore better interpreted as a ventilation-related grouping associated with seasonally dependent differences in the lower-to-middle-layer subtype distribution.

LTS and PVV show weaker and more seasonally dependent profile responses than PBLH (Fig. 4). Under low-LTS conditions, pollution- and marine-associated subtype signatures are mainly confined below 2 km. Under high-LTS conditions, several lower-level subtype signals weaken, whereas dust, polluted-dust, and elevated smoke subtypes show enhanced relative occurrence at 3–6 km. This pattern is consistent with educed boundary-layer–free-troposphere exchange under more stable lower-tropospheric conditions and with a stronger relative separation between lower-layer and elevated aerosol signals. However, this LTS-related response is seasonally dependent, with clearer positive differences aloft in spring and winter (Fig. S1). When PVV is grouped by sign, the elevated-smoke subtype shows a more pronounced 2–4 km peak under ascending-motion conditions (PVV < 0), and polluted dust subtype also shows visible ALL_FO values in the 2–4 km layer. Under subsiding-motion conditions (PVV > 0), several aerosol subtypes show stronger lower-layer relative occurrence, whereas elevated-layer signals weaken. This contrast indicates that ascending-motion backgrounds are associated with a larger elevated-layer subtype share, whereas subsiding backgrounds are associated with a larger lower-layer share.

The season-controlled redistribution metric provides a compact comparison of the five meteorological variables (Fig. 5a). PBLH has the largest redistribution strength, 31.5%, with a robust positive high-minus-low difference in 0–2 km and robust negative differences in both layers above 2 km (Fig. 5b). This identifies PBLH as the clearest boundary-layer-related indicator of vertical aerosol redistribution among the five variables. PVV has the second-largest redistribution strength, 17.4%. In Fig. 5, PVV is treated as a continuous variable and grouped into low and high categories using within-season terciles. Thus, the Fig. 5 PVV contrast represents higher-minus-lower PVV conditions within each season, not the subsidence-minus-ascent contrast used for the descriptive profiles in Fig. 4.

LTS is associated with a smaller 0–2 km share and a larger 4–8 km share under more stable lower-tropospheric conditions, whereas VC and RH show weaker and more seasonally dependent contrasts. The season-stratified analysis confirms that the PBLH-associated increase below 0–2 km and decrease aloft are the most consistent across seasons (Fig. S1). APro diagnostics show only partial optical consistency: some ALL_FO shifts correspond to changes in layer-resolved AOD fraction, but the correspondence is not one-to-one for layer-integrated extinction (Fig. S2). ALL_FO differences should therefore be interpreted primarily as relative redistribution rather than changes in absolute optical loading, aerosol mass, or pollution intensity.

3.3. *Vertical Aerosol Stratification under Different Low-Level Circulation Regimes*

The 925-hPa circulation classification is used to relate aerosol vertical structure over Shanghai to regional low-level circulation backgrounds. The composite wind and geopotential-height fields distinguish three low-level circulation regimes (Fig. 6). Type 1 is the most frequent

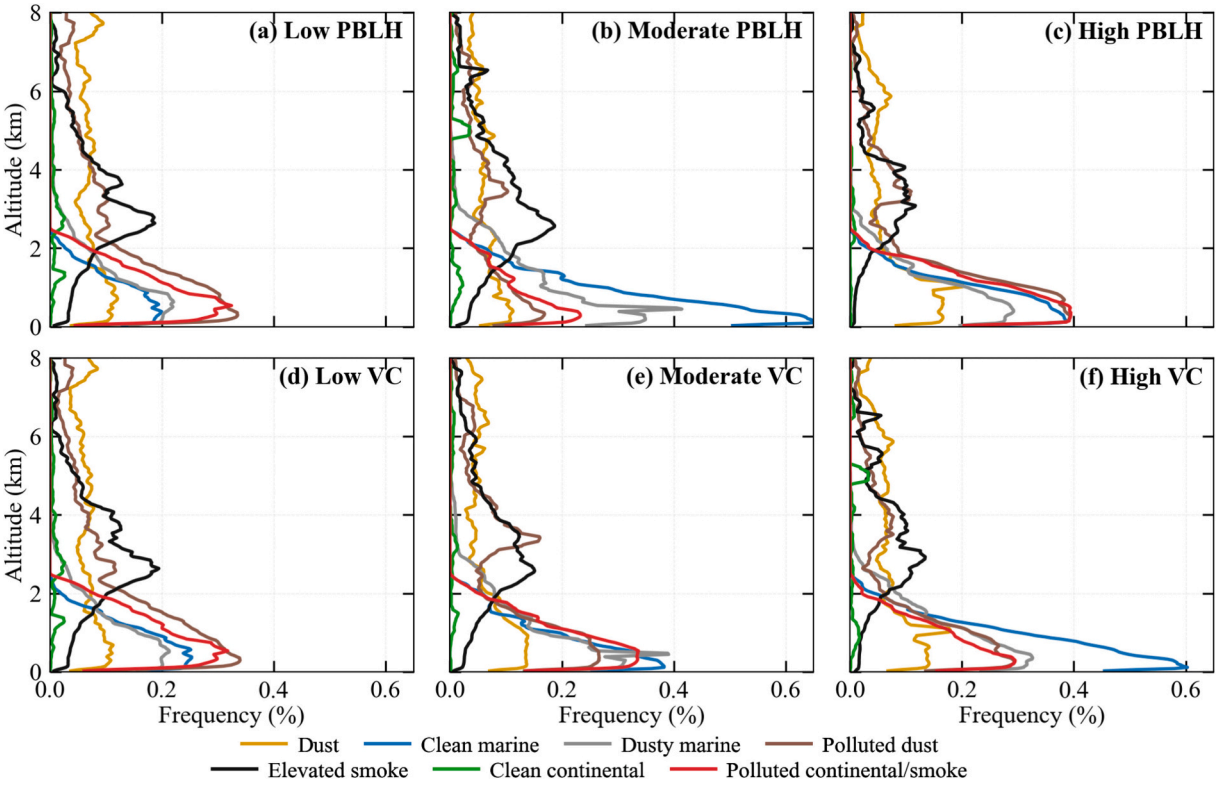


Fig. 3. Vertical profiles of aerosol subtype ALL_FO over Shanghai under different PBLH and VC conditions. (a-c) Low, moderate, and high PBLH conditions; (d-f) low, moderate, and high VC conditions.

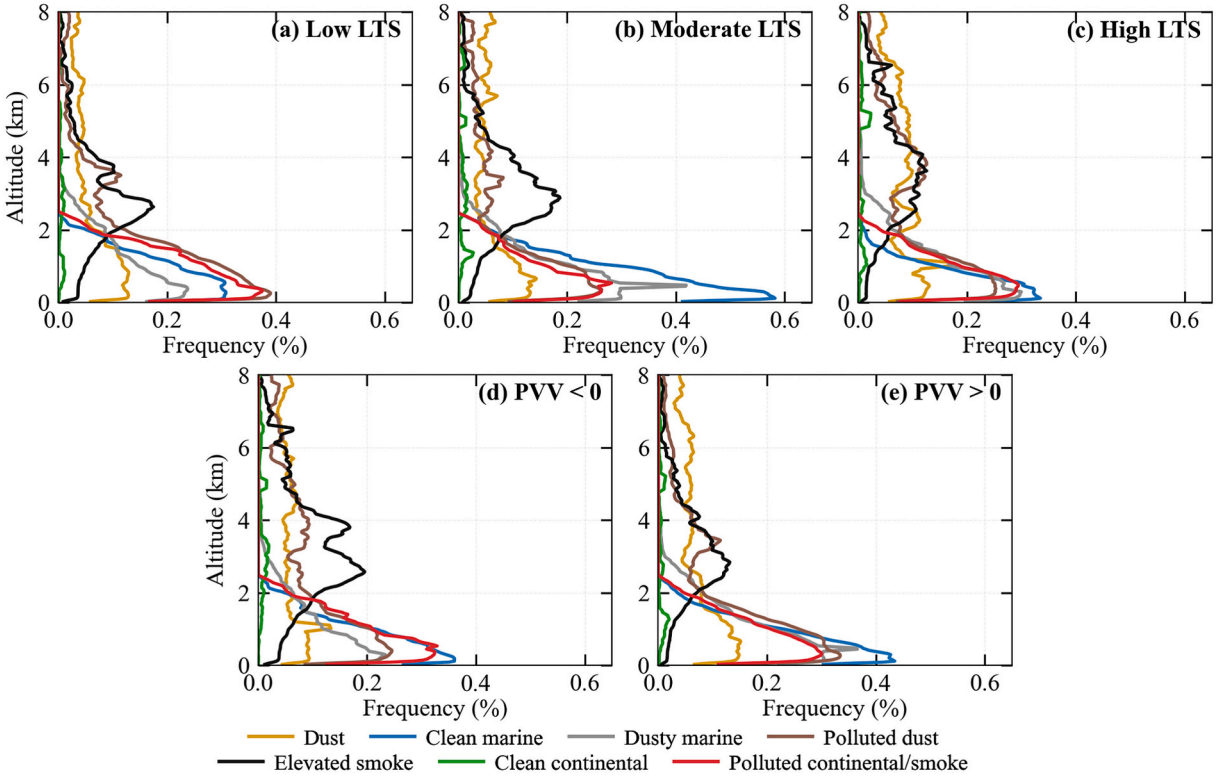


Fig. 4. Vertical profiles of aerosol subtype ALL_FO over Shanghai under different LTS and PVV conditions. (a-c) Low, moderate, and high LTS conditions; (d,e) ascending-motion (PVV < 0) and subsiding-motion (PVV > 0) conditions. Negative PVV denotes upward motion, whereas positive PVV denotes downward motion.

regime, accounting for 48.24% of all cases. Under this regime, Shanghai and the East China coastal region lie within a relatively strong

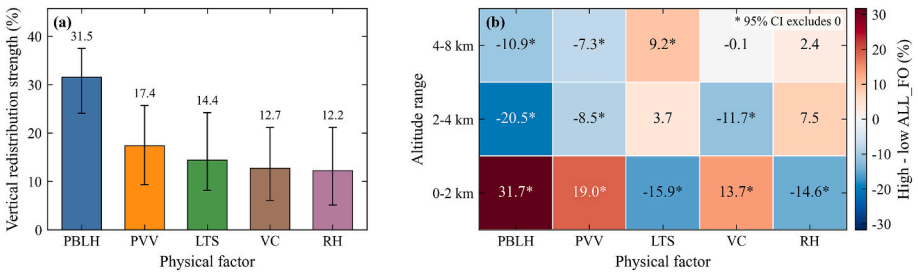


Fig. 5. Season-controlled vertical redistribution strength and high-minus-low ALL_FO differences associated with the five meteorological variables. (a) Vertical redistribution strength for each meteorological variable. Error bars indicate bootstrap 95% confidence intervals. (b) High-minus-low ALL_FO differences in the 0–2, 2–4, and 4–8 km altitude layers. Asterisks denote confidence intervals that do not include zero.

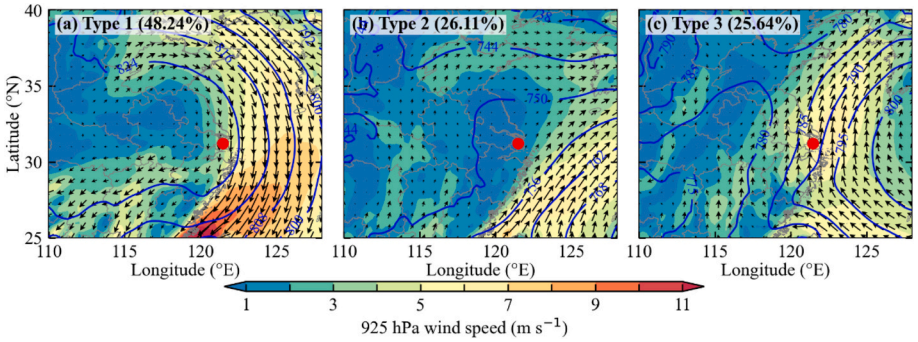


Fig. 6. Composite 925-hPa circulation patterns for the three low-level circulation regimes associated with CALIPSO overpasses within the Shanghai domain. Shading denotes 925-hPa wind speed, vectors denote 925-hPa winds, and contours denote 925-hPa geopotential height. The red dot marks Shanghai. (For interpretation of the references to colour in this figure legend, the reader is referred to the web version of this article.)

geopotential-height gradient, with northerly to northeasterly low-level wind. Type 1 is therefore interpreted as a northerly continental-transport regime. Type 2 accounts for 26.11% of all cases and is characterized by weaker low-level winds near Shanghai and a relatively flat 925-hPa geopotential-height field, and is therefore interpreted as a weak-gradient transition regime. Type 3 accounts for 25.64% of all cases and features a more evident southerly airflow corridor near Shanghai, suggesting enhanced coastal meridional transport and a southerly marine-inflow background. Overall, the three regimes broadly correspond to northerly continental transport, weak-gradient transition, and southerly marine inflow, respectively, providing a low-level synoptic context for interpreting differences in aerosol vertical structure (Shu et al., 2017; Yan et al., 2024).

Aerosol subtype profiles differ substantially among the three circulation regimes (Fig. 7). Type 1 is characterized by enhanced lower-troposphere polluted-dust signals and relatively high dust occurrence at 3–7 km, consistent with northerly transport of dust and dust–pollution mixtures from northern and northwestern China toward the YRD (Chen et al., 2023a; Sun et al., 2018). Type 2 shows the strongest elevated-smoke peak at approximately 2–3 km and weaker lower-layer polluted-dust and marine-associated shares. This elevated-smoke signal may reflect smoke-influenced regional transport and the retention of pre-existing elevated layers under weak-gradient conditions, consistent with previous lidar evidence over Shanghai and the YRD (Liu et al., 2021a; Sun et al., 2018). However, because CALIOP subtypes do not provide quantitative source apportionment and no independent fire data are used, the results do not demonstrate that biomass-burning events occur more frequently under Type 2. Type 3 exhibits enhanced clean-marine occurrence below 2 km while elevated smoke remains evident at 2–4 km, suggesting different transport influences in the lower

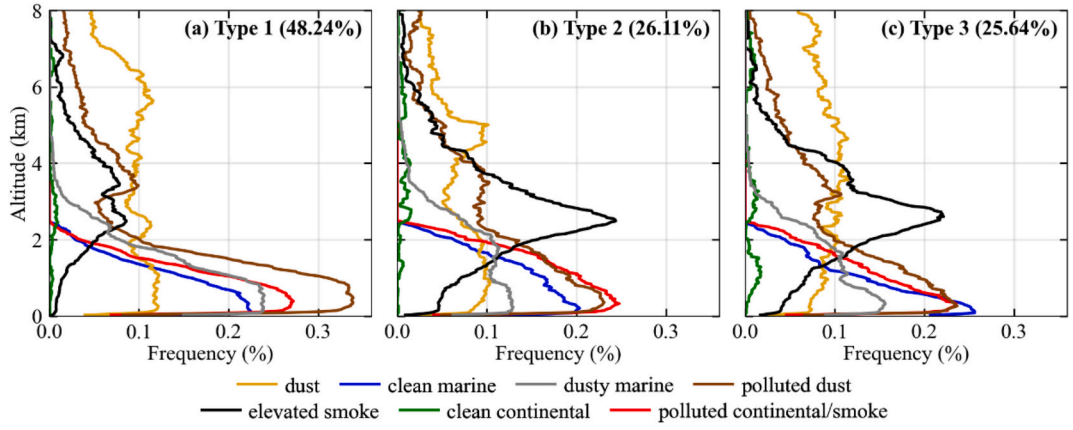


Fig. 7. Vertical profiles of CALIOP aerosol subtype ALL_FO over Shanghai under the three low-level circulation regimes.

and elevated layers. Overall, the regime-dependent profiles reflect source-region connectivity, transport direction, and circulation-dependent retention rather than source occurrence alone.

ALay-based statistics further show that the circulation regimes differ in boundary-layer-relative aerosol-layer organization (Fig. 8). Here, APB and WPB follow the layer-base classification defined in Section 2.5. In terms of profile occurrence, WPB layers are more frequent in Type 1 and Type 3, reaching 60.6% and 53.2%, respectively, whereas their occurrence is lower in Type 2 (41.7%). In contrast, APB-layer occurrence is 52.1%, 48.0%, and 50.4% for Types 1–3, respectively, showing smaller differences among the circulation regimes. Thus, APB layers are not confined to a single circulation regime but recur across different low-level backgrounds.

In terms of geometry, APB layers are centered mainly near 2.8 km, with mean layer thicknesses of 1.08–1.25 km, indicating broadly similar elevated-layer geometry across the circulation regimes. WPB layers have lower midlayer heights and mean thicknesses of 1.23–1.45 km, reflecting layers whose bases are located within or below the diagnosed boundary layer and may extend upward from the lower troposphere. The AOD_{532} distributions show that WPB layers generally have higher layer AOD_{532} than APB layers. Both APB and WPB layers also exhibit relatively larger AOD_{532} under Type 2.

Overall, Figs. 7 and 8 indicate that the circulation-regime differences are expressed mainly in aerosol subtype composition and layer optical loading, rather than in the occurrence or geometric structure of APB layers. APB layers recur under all three regimes and exhibit broadly similar heights and thicknesses, but the aerosol subtypes occupying these layers and their optical contributions differ among the circulation backgrounds.

3.4. *Height-resolved transport pathways and potential contribution regions of 2–4 km APB-Layer events*

To characterize height-dependent transport associated with 2–4 km APB-layer events, we combined trajectory clustering with height-resolved WPSCF analysis. Fig. 9 summarizes the general air-mass pathways at 500, 1500, 3000, and 6000 m, whereas Fig. S3 compares independently clustered trajectories at 2000, 3000, and 4000 m across the target layer. For the selected APB-layer events, trajectory points were classified into 0–1, 1–2, 2–4, and 4–8 km altitude bins for the WPSCF analysis.

The clustered trajectories show a progressive expansion of the upstream domain with arrival height (Fig. 9). At 500 m, most pathways remain over the YRD, the East China coastal region, and adjacent marine areas. At 1500 m, the pathways extend toward Anhui and southern North China, whereas the 3000 m trajectories are dominated by inland northwesterly-to-westerly pathways from the western YRD and southern North China. Thus, lower-level pathways are more strongly connected to nearby regional and coastal sectors, whereas pathways above 2 km have broader inland and upper-level origins. Fig. S3 shows that the principal transport directions remain broadly similar at 2000, 3000, and 4000 m, although the pathway partitioning and cluster percentages vary among the independently derived solutions.

Fig. 10 shows that the potential contribution regions vary substantially with transport altitude. WPSCF signals are sparse below 1 km and become more evident, although still discontinuous, within 1–2 km over the YRD, Anhui, Shandong, and southern North China. The most coherent region occurs in the 2–4 km layer, extending from Henan, Hubei, Anhui, and the western YRD toward Shanghai. At 4–8 km, high-WPSCF regions extend farther upstream across North China, Inner Mongolia, and northwestern China, with an additional branch over Shandong, the northern YRD, and the East China coastal sector. The complementary 4–8 km pathways farther upstream and 2–4 km pathways over central-eastern China indicate a height-dependent source–receptor association, but do not by themselves resolve vertical transfer between the two layers. Overall, the 2–4 km layer provides the clearest regional connection to Shanghai, whereas the 4–8 km layer indicates additional and more remote upstream pathways.

4. Discussion

The results show that aerosol over Shanghai is organized as a vertically structured column rather than as a simple extension of near-surface pollution. Surface PM is most directly related to aerosols within or coupled to the boundary layer, whereas AOD integrates optical contributions throughout the column. The 44.2% contribution from aerosols above 2 km therefore underscores why AOD-PM relationships depend on aerosol vertical placement and boundary-layer structure (Zhu et al., 2024a). The three-layer framework further shows that subtype occurrence, extinction, depolarization, and layer-resolved AOD provide vertically consistent information on the lower polluted/marine mixed layer, the 2–4 km elevated layer, and the 4–8 km dust-related layer. This integrated perspective complements previous CALIOP studies and provides a more process-relevant basis for evaluating model biases in aerosol vertical profiles (Bourgeois et al., 2018; Gui et al., 2021; Koffi et al., 2012).

The greater cross-season consistency of the PBLH association likely reflects its direct correspondence with the vertical redistribution examined here (Li et al., 2017; Su et al., 2018). PBLH represents the vertical extent of boundary-layer mixing and therefore provides a physically relevant reference for interpreting shifts between lower-layer and elevated aerosol-sample shares. Although the fixed 0–2, 2–4, and

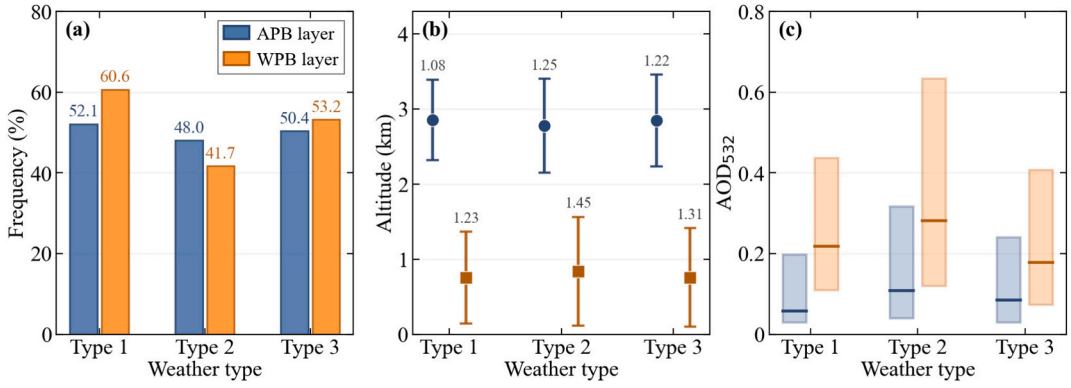


Fig. 8. Occurrence, geometric properties, and optical loading of APB and WPB layers under the three low-level circulation regimes. (a) Profile occurrence of APB and WPB layers; (b) mean layer-base to layer-top range, midlayer height, and layer thickness; and (c) distributions of layer AOD_{532}. In (b), vertical bars indicate layer-base to layer-top ranges, symbols indicate midlayer heights, and numbers denote mean layer thicknesses. In (c), boxes indicate the 25th–75th percentile range, and horizontal lines denote medians.

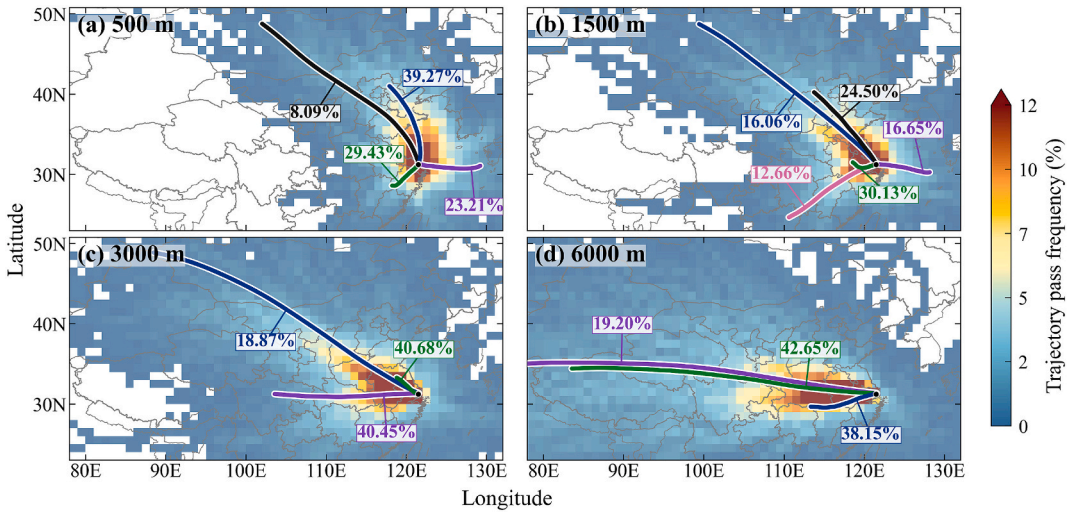


Fig. 9. Clustered 48-h HYSPLIT backward trajectories for CALIPSO overpass cases within the Shanghai domain at arrival heights of (a) 500 m, (b) 1500 m, (c) 3000 m, and (d) 6000 m. Shading denotes trajectory pass frequency, colored lines indicate clustered trajectory pathways, and percentages denote the contribution of each trajectory cluster.

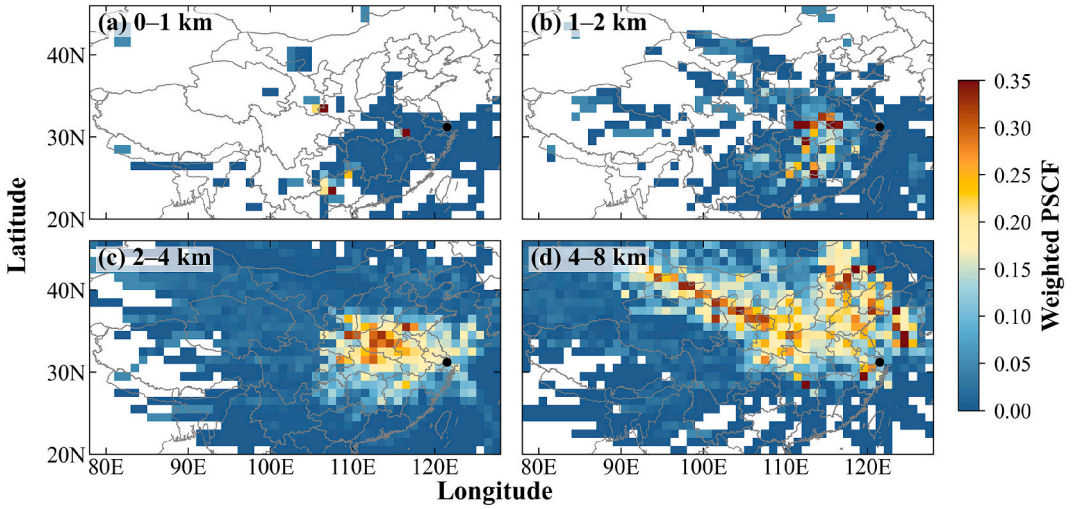


Fig. 10. Height-resolved WPSCF distributions for 2–4 km APB-layer events over Shanghai. WPSCF was calculated from trajectories initialized at 2500, 3000, and 3500 m. Panels show WPSCF values after classifying trajectory output points along the 48-h backward paths into (a) 0–1 km, (b) 1–2 km, (c) 2–4 km, and (d) 4–8 km altitude layers. The black dot marks Shanghai.

4–8 km altitude bands were defined independently from the long-term CALIOP profiles rather than from PBLH, changes in PBLH directly alter the vertical range over which lower-tropospheric aerosols can be mixed. By contrast, VC combines mixing depth and wind speed, RH is associated with competing hygroscopic-growth and removal processes, and PVV represents synoptic-scale vertical motion rather than local boundary-layer turbulence or entrainment. Their relationships with aerosol vertical structure may therefore vary more strongly with season, altitude, and circulation conditions. PBLH is thus interpreted as the most consistent statistical indicator among the variables examined, rather than as a direct causal driver or an indicator of increased aerosol loading.

The circulation-regime and WPSCF results also show that elevated aerosol layers over Shanghai cannot be explained solely by local lifting of boundary-layer pollution. The circulation regimes are associated with differences in aerosol-subtype composition and layer optical loading, while the WPSCF distributions vary with transport altitude. For 2–4 km APB-layer events, the strongest event-related signal occurs within the same altitude range, accompanied by weaker lower-level signals and additional upper-level pathways. The elevated layers are therefore associated with upstream connectivity, transport height, and their position relative to the boundary layer, consistent with previous evidence of altitude-dependent aerosol and dust transport over eastern China (Chen et al., 2023b; Fan et al., 2019; Liu et al., 2021a, 2021b).

Column AOD may not represent near-surface pollution when a substantial fraction of the optical signal lies above the boundary layer. For chemical transport and climate models, reproducing column AOD alone is insufficient if the simulated aerosol is vertically misplaced. Model intercomparisons have further shown that differences in convective-transport and boundary-layer-mixing parameterizations can substantially alter simulated vertical tracer profiles (Hoyle et al., 2011), underscoring the need to evaluate vertical placement rather than column loading alone. Errors in aerosol vertical placement, boundary-layer-relative layer position, or transport height may affect simulated aerosol radiative effects, AOD-PM relationships, and the vertical distribution of aerosol optical properties (Koffi et al., 2012). The results therefore emphasize that evaluating aerosol over coastal megacities requires a combined view of optical loading, subtype structure,

boundary-layer coupling, and height-dependent transport.

Several limitations should be noted. This study provides an observation-based statistical diagnosis rather than deterministic source apportionment. CALIOP aerosol subtypes are algorithm-derived optical classifications and not direct proxies for chemical composition or emission-source categories. Because clear-air samples are excluded, ALL_FO describes the relative partitioning of detected aerosol samples among subtypes and altitude bins. Even when overpass numbers are comparable, the number and vertical distribution of detected aerosol samples may differ among groups; ALL_FO contrasts should therefore not be interpreted as absolute changes in aerosol occurrence. APro optical quantities are additionally affected by cloud screening, signal attenuation, hygroscopic growth, and retrieval uncertainties.

The WPSCF results are also subject to trajectory and transport-process uncertainties. Backward-trajectory positions depend on the resolution and accuracy of the GDAS1 fields, and positional errors can accumulate with travel time, particularly for distant and high-altitude pathways. The three arrival heights partly represent receptor-altitude uncertainty but do not constitute a full meteorological or trajectory ensemble. Trajectory-based WPSCF cannot resolve subgrid-scale dispersion, turbulent and convective mixing, boundary-layer exchange, removal, or aerosol chemical and microphysical evolution. High-WPSCF cells therefore identify broad potential contribution regions rather than source strength or absolute contribution. Although model-based studies have shown that pollutants introduced at high altitudes can influence surface concentrations through large-scale subsidence when vertical transport is evaluated against observations (Barrett et al., 2012), the association between the 4–8 km pathways and the 2–4 km APB layer in the present study should not be interpreted as direct evidence of a resolved downward-transport process.

5. Conclusions

Using CALIOP observations from 2006 to 2023 together with ERA5 meteorological fields, objective 925-hPa circulation-regime classification, and HYSPLIT/WPSCF diagnostics, this study characterized aerosol vertical organization over Shanghai and its associations with meteorological conditions and height-resolved transpor. CALIOP identifies a persistent three-layer aerosol structure within 0–8 km. The lower layer below 2 km is characterized by pollution- and marine-associated subtype signatures and provides the dominant optical contribution. The 2–4 km layer contains a distinct elevated aerosol signal, with a 23.9% contribution to the 0–8 km aerosol optical loading and a pronounced elevated-smoke signature. The 4–8 km layer is marked by enhanced dust and polluted-dust occurrence and larger particulate depolarization. In total, aerosols above 2 km account for 44.2% of the 0–8 km optical signal, showing that elevated and middle-level aerosols are a substantial component of the aerosol column over Shanghai.

The analysis of ERA5 meteorological variables indicates that boundary-layer-relative redistribution is a key feature of the observed variability. Among the examined variables, PBLH shows the strongest and most seasonally consistent redistribution signal (31.5%), with higher PBLH associated with a larger relative aerosol-sample share below 2 km and smaller shares aloft. LTS, PVV, VC, and RH show more conditional associations with the vertical distribution, with patterns that depend on altitude and season. The circulation-regime analysis further shows that the weak-gradient transition regime has the strongest 2–4 km elevated-smoke signal and larger layer optical contributions when aerosol layers occur, while northerly continental inflow and southerly marine inflow are associated with different lower-layer subtype signatures.

Height-resolved WPSCF analysis associates the 2–4 km APB-layer events with elevated transport pathways. The most coherent event-related corridor occurs within the 2–4 km layer over Henan, Hubei, Anhui, and the western YRD. The sub-1 km signal is sparse and discontinuous, and the 4–8 km layer contains additional upstream elevated pathways. These patterns indicate that the observed elevated layers are associated with transport height, boundary-layer-relative layer position, and regional circulation background. For coastal megacities, evaluating aerosol radiative effects, AOD-surface pollution relationships, and model vertical profiles therefore requires explicit attention to aerosol-layer altitude and boundary-layer coupling.

CRediT authorship contribution statement

Fangzhi Wei: Writing – original draft, Methodology, Investigation, Conceptualization. **Tianwen Wei:** Writing – review & editing, Methodology, Data curation. **Qiuwei Xia:** Investigation, Data curation. **Yiqian Liu:** Resources, Data curation. **Xinming Zhu:** Software, Investigation. **Haiyun Xia:** Writing – review & editing, Supervision, Project administration.

Declaration of competing interest

The authors declare that they have no known competing financial interests or personal relationships that could have appeared to influence the work reported in this paper.

Appendix A. Supplementary data

Supplementary data to this article can be found online at https://doi.org/10.1016/j.atmosres.2026.109329.

Data availability

Data will be made available on request.

References

Andreae, M.O., Crutzen, P.J., 1997. Atmospheric aerosols: Biogeochemical sources and role in atmospheric chemistry. Science 276, 1052–1058. https://doi.org/10.1126/science.276.5315.1052.

Barrett, S.R.H., Yim, S.H.L., Gilmore, C.K., Murray, L.T., Kuhn, S.R., Tai, A.P.K., Yantosca, R.M., Byun, D.W., Ngan, F., Li, X., Levy, J.I., Ashok, A., Koo, J., Wong, H. M., Dessens, O., Balasubramanian, S., Fleming, G.G., Pearlson, M.N., Wollersheim, C., Malina, R., Arunachalam, S., Binkowski, F.S., Leibensperger, E.M., Jacob, D.J., Hileman, J.I., Waitz, I.A., 2012. Public health, climate, and economic impacts of desulfurizing jet fuel. Environ. Sci. Technol. 46, 4275–4282. https://doi.org/10.1021/es203325a.

Bourgeois, Q., Ekman, A.M.L., Renard, J.-B., Krejci, R., Devasthale, A., Bender, F.A.-M., Riipinen, I., Berthet, G., Tackett, J.L., 2018. How much of the global aerosol optical depth is found in the boundary layer and free troposphere? Atmos. Chem. Phys. 18, 7709–7720. https://doi.org/10.5194/acp-18-7709-2018.

Chang, W., Zhan, J., 2017. The association of weather patterns with haze episodes: recognition by $PM_{2.5}$ oriented circulation classification applied in Xiamen, Southeastern China. Atmos. Res. 197, 425–436. https://doi.org/10.1016/j.atmosres.2017.07.024.

Chen, B., Dong, L., Huang, J., Wang, Y., Jing, Z., Yan, W., Wang, X., Song, Z., Huang, Z., Guan, X., Dong, X., Huang, Y., 2023a. Analysis of long-term trends in the vertical distribution and transport paths of atmospheric aerosols in typical regions of China using 15 years of CALIOP data. JGR Atmospheres 128, e2022JD038066. https://doi.org/10.1029/2022JD038066.

Chen, Y.-C., Tseng, W.-L., Wu, C.-M., Chen, W.-T., Chang, C.-H., Tseng, H.-Y., 2023b. Influence of synoptic weather on aerosol variability over East Asia: present and future. Atmos. Res. 295, 107023. https://doi.org/10.1016/j.atmosres.2023.107023.

Dimitriou, K., Grivas, G., Liakakou, E., Gerasopoulos, E., Mihalopoulos, N., 2021. Assessing the contribution of regional sources to urban air pollution by applying 3D-PSCF modeling. Atmos. Res. 248, 105187. https://doi.org/10.1016/j.atmosres.2020.105187.

Fan, W., Qin, K., Xu, J., Yuan, L., Li, D., Jin, Z., Zhang, K., 2019. Aerosol vertical distribution and sources estimation at a site of the Yangtze River Delta region of China. Atmos. Res. 217, 128–136. https://doi.org/10.1016/j.atmosres.2018.11.002.

Gui, K., Che, H., Zheng, Y., Zhao, H., Yao, W., Li, L., Zhang, L., Wang, H., Wang, Y., Zhang, X., 2021. Three-dimensional climatology, trends, and meteorological drivers of global and regional tropospheric type-dependent aerosols: Insights from 13 years (2007–2019) of CALIOP observations. Atmos. Chem. Phys. 21, 15309–15336. https://doi.org/10.5194/acp-21-15309-2021.

Guo, J., Liu, H., Wang, F., Huang, J., Xia, F., Lou, M., Wu, Y., Jiang, J.H., Xie, T., Zhaxi, Y., Yung, Y.L., 2016. Three-dimensional structure of aerosol in China: a perspective from multi-satellite observations. Atmos. Res. 178–179, 580–589. https://doi.org/10.1016/j.atmosres.2016.05.010.

Haywood, J., Boucher, O., 2000. Estimates of the direct and indirect radiative forcing due to tropospheric aerosols: a review. Rev. Geophys. 38, 513–543. https://doi.org/10.1029/1999RG000078.

He, B., Yu, G., Zhang, X., He, Z., Wang, Q., Liu, Q., Mao, J., Zhang, Y., 2022. Contributions of regional transport versus local emissions and their retention effects during $PM_{2.5}$ pollution under various stable weather in Shanghai. Front. Environ. Sci. 10, 858685. https://doi.org/10.3389/fenvs.2022.858685.

He, Q., Wang, M., Yim, S.H.L., 2021. The spatiotemporal relationship between $PM_{2.5}$ and aerosol optical depth in China: Influencing factors and implications for satellite $PM_{2.5}$ estimations using MAIAC aerosol optical depth. Atmos. Chem. Phys. 21, 18375–18391. https://doi.org/10.5194/acp-21-18375-2021.

Hersbach, H., Bell, B., Berrisford, P., Hirahara, S., Horányi, A., Muñoz-Sabater, J., Nicolas, J., Peubey, C., Radu, R., Schepers, D., Simmons, A., Soci, C., Abdalla, S., Abellan, X., Balsamo, G., Bechtold, P., Biavati, G., Bidlot, J., Bonavita, M., De Chiara, G., Dahlgren, P., Dee, D., Diamantakis, M., Dragani, R., Flemming, J., Forbes, R., Fuentes, M., Geer, A., Haimberger, L., Healy, S., Hogan, R.J., Hólm, E., Janisková, M., Keeley, S., Laloyaux, P., Lopez, P., Lupu, C., Radnoti, G., De Rosnay, P., Rozum, I., Vamborg, F., Villaume, S., Thépaut, J., 2020. The ERA5 global reanalysis. Quart. J. Royal Meteorol. Soc. 146, 1999–2049. https://doi.org/10.1002/qj.3803.

Hoyle, C.R., Marécal, V., Russo, M.R., Allen, G., Arteta, J., Chemel, C., Chipperfield, M.P., D'Amato, F., Dessens, O., Feng, W., Hamilton, J.F., Harris, N.R.P., Hosking, J.S., Lewis, A.C., Morgenstern, O., Peter, T., Pyle, J.A., Reddmann, T., Richards, N.A.D., Telford, P.J., Tian, W., Viciani, S., Volz-Thomas, A., Wild, O., Yang, X., Zeng, G., 2011. Representation of tropical deep convection in atmospheric models – part 2: Tracer transport. Atmos. Chem. Phys. 11, 8103–8131. https://doi.org/10.5194/acp-11-8103-2011.

Hu, Y., Tan, J., Grimmond, S., Ao, X., Yan, Y., Liu, D., 2022. Observed and modeled urban heat island and sea-breeze circulation interactions: a Shanghai case study. J. Appl. Meteorol. Climatol. 61, 239–259. https://doi.org/10.1175/JAMC-D-20-0246.1.

Jing, D., He, Y., Yin, Z., Huang, K., Liu, F., Yi, F., 2025. Evolution of tropospheric aerosols over Central China during 2010–2024 as observed by lidar. Atmos. Chem. Phys. 25, 17047–17067. https://doi.org/10.5194/acp-25-17047-2025.

Kaufman, Y.J., Tanré, D., Boucher, O., 2002. A satellite view of aerosols in the climate system. Nature 419, 215–223. https://doi.org/10.1038/nature01091.

Kim, I.S., Wee, D., Kim, Y.P., Lee, J.Y., 2016. Development and application of three-dimensional potential source contribution function (3D-PSCF). Environ. Sci. Pollut. Res. 23, 16946–16954. https://doi.org/10.1007/s11356-016-6787-x.

Kim, M.-H., Omar, A.H., Tackett, J.L., Vaughan, M.A., Winker, D.M., Trepte, C.R., Hu, Y., Liu, Z., Poole, L.R., Pitts, M.C., Kar, J., Magill, B.E., 2018. The CALIPSO version 4 automated aerosol classification and lidar ratio selection algorithm. Atmos. Meas. Tech. 11, 6107–6135. https://doi.org/10.5194/amt-11-6107-2018.

Koffi, B., Schulz, M., Bréon, F., Griesfeller, J., Winker, D., Balkanski, Y., Bauer, S., Berntsen, T., Chin, M., Collins, W.D., Dentener, F., Diehl, T., Easter, R., Ghan, S., Ginoux, P., Gong, S., Horowitz, L.W., Iversen, T., Kirkevåg, A., Koch, D., Krol, M., Myhre, G., Stier, P., Takemura, T., 2012. Application of the CALIOP layer product to evaluate the vertical distribution of aerosols estimated by global models: AeroCom phase I results. J. Geophys. Res. 117, D10201. https://doi.org/10.1029/2011JD016858.

Li, Z., Guo, J., Ding, A., Liao, H., Liu, J., Sun, Y., Wang, T., Xue, H., Zhang, H., Zhu, B., 2017. Aerosol and boundary-layer interactions and impact on air quality. Natl. Sci. Rev. 4, 810–833. https://doi.org/10.1093/nsr/nwx117.

Liu, N., Zhou, S., Liu, C., Guo, J., 2019. Synoptic circulation pattern and boundary layer structure associated with $PM_{2.5}$ during wintertime haze pollution episodes in Shanghai. Atmos. Res. 228, 186–195. https://doi.org/10.1016/j.atmosres.2019.06.001.

Liu, Q., Wang, Y., Kuang, Z., Fang, S., Chen, Y., Kang, Y., Zhang, H., Wang, D., Fu, Y., 2016. Vertical distributions of aerosol optical properties during haze and floating dust weather in Shanghai. J. Meteorol. Res. 30, 598–613. https://doi.org/10.1007/s13351-016-5092-4.

Liu, T., He, Q., Chen, Y., Liu, J., Liu, Q., Gao, W., Huang, G., Shi, W., Yu, X., 2021a. Long-term variation in aerosol lidar ratio in Shanghai based on raman lidar measurements. Atmos. Chem. Phys. 21, 5377–5391. https://doi.org/10.5194/acp-21-5377-2021.

Liu, Y., Lin, T., Hong, J., Wang, Y., Shi, L., Huang, Y., Wu, X., Zhou, H., Zhang, J., De Leeuw, G., 2021b. Multi-dimensional satellite observations of aerosol properties and aerosol types over three major urban clusters in eastern China. Atmos. Chem. Phys. 21, 12331–12358. https://doi.org/10.5194/acp-21-12331-2021.

Liu, Z., Vaughan, M., Winker, D., Kittaka, C., Getzewich, B., Kuehn, R., Omar, A., Powell, K., Trepte, C., Hostetler, C., 2009. The CALIPSO lidar cloud and aerosol discrimination: Version 2 algorithm and initial assessment of performance. J. Atmos. Oceanic Tech. 26, 1198–1213. https://doi.org/10.1175/2009JTECHA1229.1.

Lu, D., Li, H., Tian, M., Wang, G., Qin, X., Zhao, N., Huo, J., Yang, F., Lin, Y., Chen, J., Fu, Q., Duan, Y., Dong, X., Deng, C., Abdullaev, S.F., Huang, K., 2023. Secondary aerosol formation during a special dust transport event: impacts from unusually enhanced ozone and dust backflows over the ocean. Atmos. Chem. Phys. 23, 13853–13868. https://doi.org/10.5194/acp-23-13853-2023.

Mülmenstädt, J., Feingold, G., 2018. The radiative forcing of aerosol–cloud interactions in liquid clouds: Wrestling and embracing uncertainty. Curr. Clim. Chang. Rep. 4, 23–40. https://doi.org/10.1007/s40641-018-0089-y.

Polissar, A.V., Hopke, P.K., Harris, J.M., 2001. Source regions for atmospheric aerosol measured at Barrow, Alaska. Environ. Sci. Technol. 35, 4214–4226. https://doi.org/10.1021/es0107529.

Reddy, K.R.O., Zhang, X., Bi, L., 2019. Seasonal aerosol variations over a coastal city, Zhoushan, China from CALIPSO observations. Atmos. Res. 218, 117–128. https://doi.org/10.1016/j.atmosres.2018.11.011.

Samset, B.H., Myhre, G., Schulz, M., Balkanski, Y., Bauer, S., Berntsen, T.K., Bian, H., Bellouin, N., Diehl, T., Easter, R.C., Ghan, S.J., Iversen, T., Kinne, S., Kirkevåg, A., Lamarque, J.-F., Lin, G., Liu, X., Penner, J.E., Seland, Ø., Skeie, R.B., Stier, P., Takemura, T., Tsigaridis, K., Zhang, K., 2013. Black carbon vertical profiles strongly affect its radiative forcing uncertainty. Atmos. Chem. Phys. 13, 2423–2434. https://doi.org/10.5194/acp-13-2423-2013.

Shen, L., Zhao, C., Ma, Z., Li, Z., Li, J., Wang, K., 2019. Observed decrease of summer sea-land breeze in Shanghai from 1994 to 2014 and its association with urbanization. Atmos. Res. 227, 198–209. https://doi.org/10.1016/j.atmosres.2019.05.007.

Shu, L., Xie, M., Gao, D., Wang, T., Fang, D., Liu, Q., Huang, A., Peng, L., 2017. Regional severe particle pollution and its association with synoptic weather patterns in the Yangtze River Delta region, China. Atmos. Chem. Phys. 17, 12871–12891. https://doi.org/10.5194/acp-17-12871-2017.

Stein, A.F., Draxler, R.R., Rolph, G.D., Stunder, B.J.B., Cohen, M.D., Ngan, F., 2015. NOAA'S HYSPLIT atmospheric transport and dispersion modeling system. Bull. Am. Meteorol. Soc. 96, 2059–2077. https://doi.org/10.1175/BAMS-D-14-00110.1.

Su, T., Li, Z., Kahn, R., 2018. Relationships between the planetary boundary layer height and surface pollutants derived from lidar observations over China: regional pattern and influencing factors. Atmos. Chem. Phys. 18, 15921–15935. https://doi.org/10.5194/acp-18-15921-2018.

Sun, T., Che, H., Qi, B., Wang, Y., Dong, Y., Xia, X., Wang, H., Gui, K., Zheng, Y., Zhao, H., Ma, Q., Du, R., Zhang, X., 2018. Aerosol optical characteristics and their vertical distributions under enhanced haze pollution events: effect of the regional transport of different aerosol types over eastern China. Atmos. Chem. Phys. 18, 2949–2971. https://doi.org/10.5194/acp-18-2949-2018.

Tian, P., Cao, X., Zhang, L., Sun, N., Sun, L., Logan, T., Shi, J., Wang, Y., Ji, Y., Lin, Y., Huang, Z., Zhou, T., Shi, Y., Zhang, R., 2017. Aerosol vertical distribution and optical properties over China from long-term satellite and ground-based remote sensing. Atmos. Chem. Phys. 17, 2509–2523. https://doi.org/10.5194/acp-17-2509-2017.

Wang, J., Christopher, S.A., 2003. Intercomparison between satellite-derived aerosol optical thickness and PM2.5 mass: implications for air quality studies. Geophys. Res. Lett. 30, 2095. https://doi.org/10.1029/2003GL018174.

Wang, L., Lyu, B., Bai, Y., 2020. Aerosol vertical profile variations with seasons, air mass movements and local $PM_{2.5}$ levels in three large China cities. Atmos. Environ. 224, 117329. https://doi.org/10.1016/j.atmosenv.2020.117329.

Winker, D.M., Vaughan, M.A., Omar, A., Hu, Y., Powell, K.A., Liu, Z., Hunt, W.H., Young, S.A., 2009. Overview of the CALIPSO mission and CALIOP data processing algorithms. J. Atmos. Oceanic Tech. 26, 2310–2323. https://doi.org/10.1175/2009JTECHA1281.1.

Winker, D.M., Tackett, J.L., Getzewich, B.J., Liu, Z., Vaughan, M.A., Rogers, R.R., 2013. The global 3-D distribution of tropospheric aerosols as characterized by CALIOP. Atmos. Chem. Phys. 13, 3345–3361. https://doi.org/10.5194/acp-13-3345-2013.

Wood, R., Bretherton, C.S., 2006. On the relationship between stratiform low cloud cover and lower-tropospheric stability. J. Climate 19, 6425–6432. https://doi.org/10.1175/JCLI3988.1.

Wu, B., Chen, J., Wu, N., Adili, A., Ge, Y., Abuduwaili, J., 2025. Spatiotemporal features and optical properties of aerosols in the Ili Basin: a CALIPSO-based analysis (2008–2022). Atmos. Pollut. Res. 16, 102395. https://doi.org/10.1016/j.apr.2024.102395.

Yan, F., Su, H., Cheng, Y., Huang, R., Liao, H., Yang, T., Zhu, Y., Zhang, S., Sheng, L., Kou, W., Zeng, X., Xiang, S., Yao, X., Gao, H., Gao, Y., 2024. Frequent haze events associated with transport and stagnation over the corridor between the North China Plain and Yangtze River Delta. Atmos. Chem. Phys. 24, 2365–2376. https://doi.org/10.5194/acp-24-2365-2024.

Young, S.A., Vaughan, M.A., 2009. The retrieval of profiles of particulate extinction from cloud-aerosol lidar infrared pathfinder satellite observations (CALIPSO) data: Algorithm description. J. Atmos. Oceanic Tech. 26, 1105–1119. https://doi.org/10.1175/2008JTECHA1221.1.

Zha, C., Bu, L., Li, Z., Wang, Q., Mubarak, A., Liyanage, P., Liu, J., Chen, W., 2024. Aerosol optical property measurement using the orbiting high-spectral-resolution lidar on board the DQ-1 satellite: Retrieval and validation. Atmos. Meas. Tech. 17, 4425–4443. https://doi.org/10.5194/amt-17-4425-2024.

Zhu, H., Martin, R.V., Van Donkelaar, A., Hammer, M.S., Li, C., Meng, J., Oxford, C.R., Liu, X., Li, Y., Zhang, D., Singh, I., Lyapustin, A., 2024b. Importance of aerosol composition and aerosol vertical profiles in global spatial variation in the relationship between $PM_{2.5}$ and aerosol optical depth. Atmos. Chem. Phys. 24, 11565–11584. https://doi.org/10.5194/acp-24-11565-2024.

Zhu, Z., Li, H., Fan, S., Xu, W., Fang, R., Liu, B., Gong, W., 2024a. The covariability between temperature inversions and aerosol vertical distribution over China. Atmos. Pollut. Res. 15, 101959. https://doi.org/10.1016/j.apr.2023.101959.

Zong, L., Yang, Y., Xia, H., Yuan, J., Guo, M., 2023. Elucidating the impacts of various atmospheric ventilation conditions on local and transboundary ozone pollution patterns: a case study of Beijing, China. J. Geophys. Res. Atmos. 128, e2023JD039141. https://doi.org/10.1029/2023jd039141.